Vilnius University
Faculty of Physics

Fariha Binte Rahman

Building Plasmonic Crystals from Gold Nanoimprinted Metasurfaces

Master Thesis

Laser Technology Program

Student	Fariha Binte Rahman
Supervisor	Prof. Crina Cojocaru
Co-supervisor	Dr. Agustin Mihi (ICMAB-CSIC)
Consultant	Dr. Viktorija Tamulienė
Director of Institute	Dr. Dalia Kaškelytė

Vilnius 2023

Contents

List of Abbreviations

- LSPR- Localized surface plasmon resonance
- SLR- Surface lattice resonance
- SHG- Second harmonic generation
- FIB- Focused ion beam
- NIL- Nanoimprint lithography
- PSP- Propagating surface plasmon
- LSP- Localized surface plasmon
- SFG- Sum frequency generation
- DFG- Difference frequency generation
- THG- Third harmonic generation
- FWM- Four wave mixing
- IPA- Isopropyl alcohol
- FTIR- Fourier-transform infrared
- PMT- Photo multiplier tube
- TE/TM- Transverse electric/transverse magnetic
- BBO- Barium borate
- PDMS- Polydimethylsiloxane
- FWHM- Full width at half maxima
- SEM- Scanning electron microscopy

Introduction

Metamaterials are materials with basic unit structures that have subwavelength dimensions [1]. They have been a field of interest due to their ability to manipulate physical and optical properties beyond natural materials. Instead of the properties of the material they are made of, metamaterial properties are largely defined by their structural features. Due to the ease of fabrication and characterization, the two-dimensional counterpart of metamaterials, metasurfaces are gaining more popularity by the day. In plasmonic metasurfaces, the optical properties are highly tunable due to two different effects: the local surface plasmon resonance (LSPR) and the surface lattice resonance (SLR), creating a local electric field enhancement. LSPR arises because of the coupling between the near electric field between nanoparticles, while SLR arises from the periodicity of the array itself, and can be tuned by changing the geometric features of the nanoarray. SLRs are useful in the far field because they combine the diffractive modes from two different plasmonic objects to generate a higher field enhancement.

Due to the ability to confine light in dimensions below the diffraction limit, metasurfaces also inevitably made their way to nonlinear regime. After the invention of photonic crystals, the field of frequency conversion at the nanoscale has been gradually gaining popularity through using multiple features to manipulate the resonances to enhance the electromagnetic field [2]. In the visible and IR range, the nonlinear plasmonic properties obtained in metal surface makes metasurfaces excellent candidate to achieve efficient frequency conversion [3]. In case of plasmonic structures, the existence of local field enhancement and generation of hot-spots at the edge of metal points can help generate higher harmonics for a fractional fundamental frequency power of GW/cm^2 [4], consequently giving rise to a new research field called nonlinear plasmonics. While a popular method to observe high second harmonic generation (SHG) has been to use plasmonic effects in conjugation with inherently nonlinear materials, nowadays the properties of the plasmonic metal along with subsequent patterning are being investigated as an efficient second harmonic generator. The exact origin of harmonic generation in metal remains to be explored, however, the experimental observation and correlation between the linear and nonlinear spectra give us a qualitative idea about the behaviour of the structure.

The nanostructures used in nonlinear plasmonics are usually produced by using a sequence of rather complicated fabrication processes, like e-beam lithography, focused ion beam (FIB) milling, two-photon lithography, etching, lift-off etc [5–7]. Nanoimprint lithography (NIL) is the new emerging technology which is gaining more popularity as this reduces the fabrication complexity, cost and allows increased ability to manipulate the geometrical properties of the fabricated structures.

The main objective of this master thesis work is to design and fabricate 2D periodic meta-

surfaces, using the nanoimprint method on gold. These structures show plasmonic resonances that localize the electromagnetic field near the surface. To prove this localization we plan to determine the second and third harmonic generation and to optimize the structure through manipulating its geometrical features to obtain a higher frequency conversion efficiency.

The main tasks of this work are:

- Designing nanostructures supporting intense resonances.
- Fabrication of those metasurfaces using soft nanoimprint lithography (NIL).
- Optical characterization of the fabricated metasurfaces.
- Generate and detect the second (and third) harmonics in the metasurface.
- Optimizing the metasurface properties to obtain higher light-matter interaction.

1 Literature Overview

1.1 Plasmon Resonances

The definition of plasmons in modern literature can be as follows: "plasmon is a quantum quasi-particle representing the elementary excitation, or modes, of the charge density oscillations in a plasma" [8]. In the free electron plasma, the electron cloud oscillates at an interaction with an incident electromagnetic (EM) wave. This oscillation energy impacts both the electromagnetic wave and the free electron excitation, giving rise to a perturbation which is neither photon nor plasmon. This hybrid modes are called plasmon-polaritons and they rise at a metal-dielectric interface [9]. Surface plasmon-polaritons can be divided into two categories: namely localized and propagating surface plasmon-polaritons. And in both of these cases, the maximum coupling between the incident EM wave and inherent free electron oscillation can be reached at a specific resonance condition.

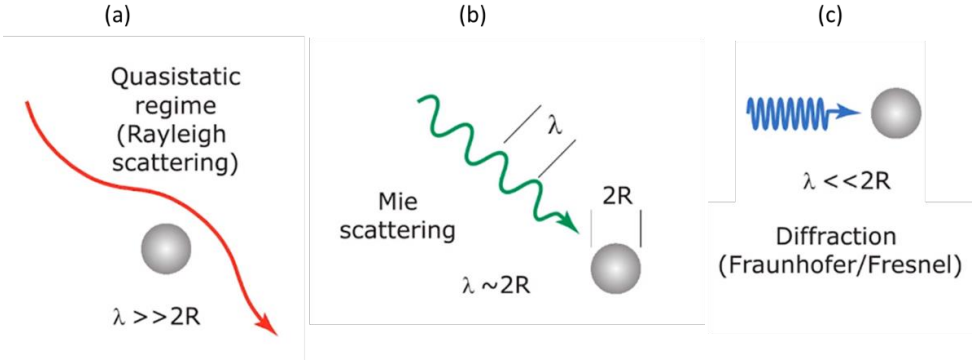

Figure 1. *Interaction mechanisms between nanoparticles and oscillating electromagnetic field, (a) Quasi-static regime when the incident wavelength is much higher than the object size (b) Mie scattering regime, when the object size is comparable to the incident wavelength and (c) Fraunhofer diffraction when the scattering object is much larger than the incoming wavelength.*

For the simplest problem of an isolated nanoparticle in an electromagnetic field, we move to the quasi-static regime when the radius of the particle is much smaller than the incident wavelength (Figure 1 (a)). In this regime, because of the particle size we can ignore the spatial variation in the electromagnetic field. In this case, the electromagnetic field inside the particle can be expressed as a constant value, depending on the incident electromagnetic field E_0 and it can be expressed as:

$$E_{in} = \frac{3\epsilon_m}{\epsilon(\omega) + 2\epsilon_m} E_0 \tag{1}$$

Where ϵ_m is the permittivity of the medium, ϵ is the permittivity of the metal itself which varies with the incident frequency, ω. In Equation (1), if the denominator is zero, we have infinite

field inside the particle. In standard dielectrics it's not possible, as the permittivity constant of those are mostly between 1 and 10. However, when we consider metals, it's possible to have a wavelength range where the absorption is small (consequently the imaginary part of permittivity is almost zero) and no wave propagation is allowed inside the material (the real part is less than zero). Therefore in metals it is possible to have much larger field than the incoming field, making them excellent plasmonic materials. Apart from metals, materials with sufficient carrier density like Indium Tin Oxide (ITO) [10] or some specific doped semiconductors [11] can also work as plasmonic materials.

1.1.1 Propagating Surface Plasmon (PSP)

Propagating surface plasmons are defined as the surface electromagnetic waves that can be supported at the metal/dielectric interface. Because PSPs are related to the collective oscillation of the free electron cloud in the metal through coherent binding, they have a greater momentum than a free photon. Thus PSPs must follow some form of momentum matching technique to get excited. These techniques often include prism coupling [12] or grating coupling [13] (Figure 2). A detailed review of PSPs can be found in [14, 15].

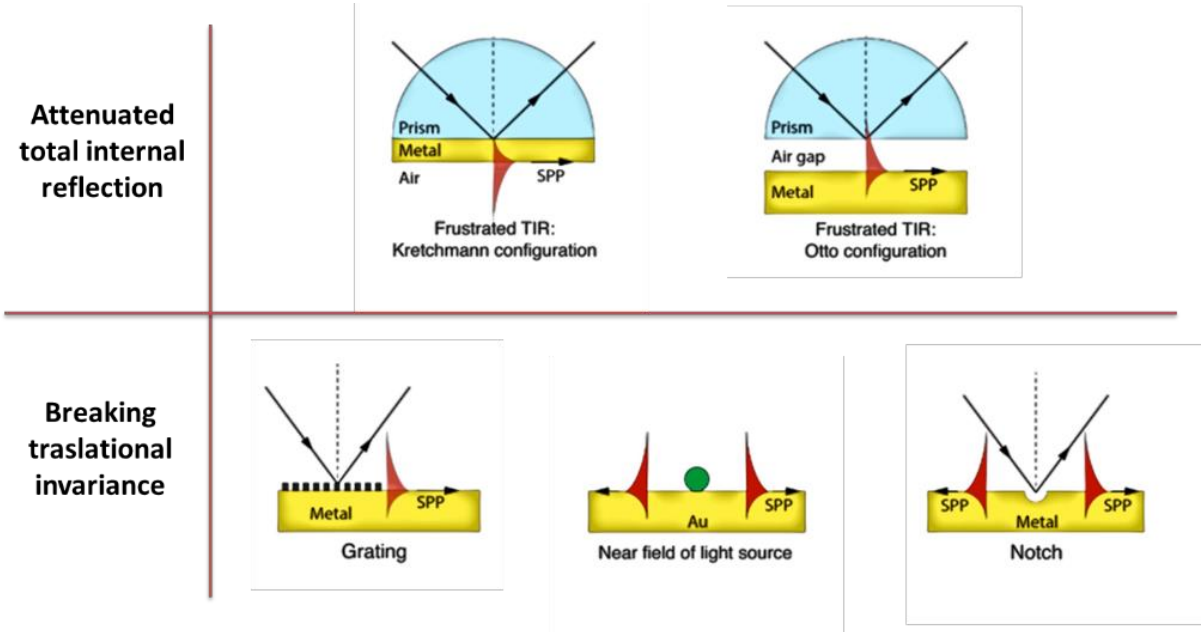

Figure 2. *Commonly used PSP excitation methods.*

1.1.2 Localized Surface Plasmon (LSP)

On the other hand, localized surface plasmons are combined oscillation of the free electrons in a metal nanoparticle. Unlike PSPs, they do not have a specific propagation direction, instead show a strong coupling to the incident electromagnetic field.

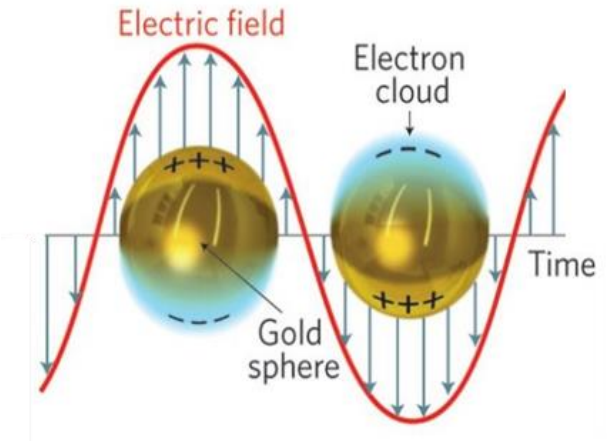

Figure 3. *Schematic representation of an electron cloud associated with a metal nanoparticle.*

The energy involved in this process can be dissipated both as heat within the nanoparticle or be radiated back into free space. From a more macroscopic point of view, LSPs can be then explained in terms of their absorption and scattering properties. The scattering and absorption cross sections can be described by the following formulas:

$$\sigma_{abs} \propto 4\pi r \mathrm{Im} \frac{\epsilon - \epsilon_m}{\epsilon + 2\epsilon_m} \tag{2}$$

$$\sigma_{scat} \propto \frac{8\pi}{3} r^4 \left| \frac{\epsilon - \epsilon_m}{\epsilon + 2\epsilon_m} \right|^2 \tag{3}$$

Here σ denotes the cross-sections, r is the nanoparticle radius and ϵ_m and ϵ are the permittivity of the medium and the metal, respectively. A careful observation of the equations show us that compared to absorption, the scattering depends more heavily on the nanoparticle size. The nanoparticle shape also plays a key role in determining the localized plasmon response. Asymmetric modes give rise to multiple dipolar modes, making the optical response much more complex [16].

1.2 Arrays of Plasmonic Nanoparticles: Surface Lattice Resonance

The quality of localized plasmon resonance improves significantly when involved with far-field coupling. For a randomly scattered assembly of particles, the scattered fields from the

nanoparticles due to impinging electromagnetic field are also random and has no particular phase relationship. However, if the particles are arranged in a periodic fashion and the period is comparable to the wavelength of the incident light, the array acts as a diffraction grating, resulting in constructive interference pattern. In this case, the LSPR of the particles decides the scattering by acting as the oscillator and the periodicity of the array fixes the wavelength at which the constructive interference occurs. These are called diffractively coupled localized plasmon resonances, or surface lattice resonances (SLR). While the diffraction is evident in arrays of any materials (dielectrics, metals), the plasmonic oscillator provides a much higher coupling effects arising from the nanoparticle polarizability. A proper choice of nanoparticle size and shape along with the array periodicity thus gives much flexibility in terms of tuning the plasmonic response, and it improves the quality factor of the resonance as well.

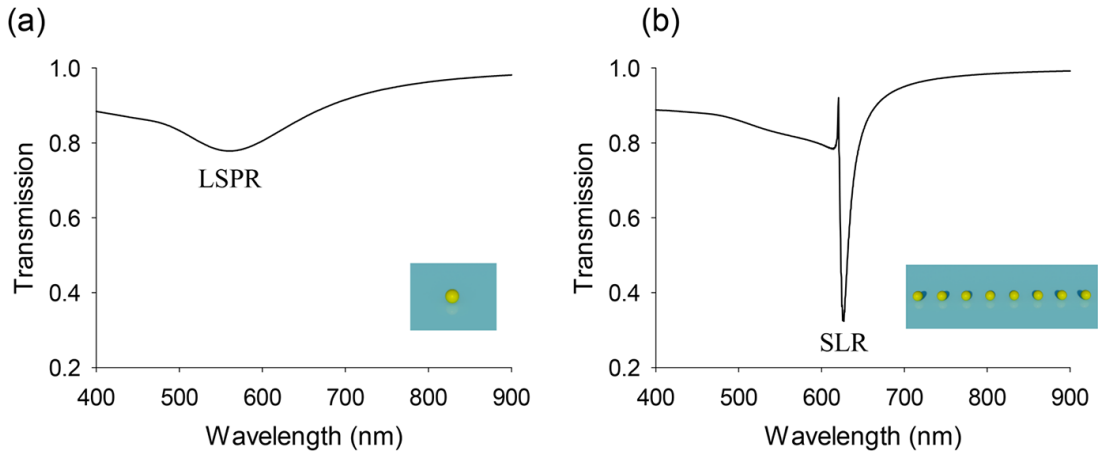

Figure 4. *Optical transmission spectra for (a) a single nanoparticle and (b) a 1D periodic chain of nanoparticles of size 80nm. The periodic chain shows a significant improvement in the resonance quality. Reproduced from [17].*

These diffractively coupled modes occur when the resonance is close to a Rayleigh anomaly wavelength of the system. Rayleigh anomaly refers to the wave that graze the grating plane and at this wavelength the modes transition into propagating from evanescent waves [18]. For the diffracted wave that is related to the normal incidence, the resonance is the strongest. However, when considering 2D gratings, there are mode overlaps and resonance broadening as well. For a general case of square 2D grating, the Rayleigh anomaly position of the (m,n)th order can be determined from the formula:

$$\lambda_{m,n} = L\frac{\sqrt{\eta_2{}^2(m^2+n^2) - \eta_1{}^2 p^2 \sin\theta} \pm m\eta_1 \sin\theta}{m^2+n^2} \tag{4}$$

where $\lambda_{m,n}$ is the wavelength of the (m,n)th resonance, L is the lattice period, η_1 and η_2 are the refractive indices of the dielectric media on both sides of the grating, and θ is the angle of

incidence. So by changing these parameters we can manipulate the Rayleigh wavelengths.

1.3 SHG in Plasmonic Structures

Nonlinear effects are seen as a consequence of the polarization P responding nonlinearly to the incident light. When a light of fundamental frequency ω and electric field E hits a material, the polarization P in the material is defined by the following equation:

$$P = \epsilon_0(\chi^{(1)}E + \chi^{(2)}E^2 + \chi^{(3)}E^3 + ... + \chi^{(n)}E^n) \tag{5}$$

where ϵ_0 is the electrical permittivity of the material in vacuum, $\chi^{(n)}$ is the n-th order susceptibility, which is a tensor of rank (n+1) [19]. The nonlinear susceptibilities, i.e., $\chi^{(2)}, \chi^{(3)}$ are usually very small compared to the linear one. However, under intense incident field, the nonlinear susceptibility contribution in the polarization can get significant, and it acts as a source for generating new frequencies. The second term in Equation (5) gives rise to second order nonlinear phenomena such as second harmonic generation (SHG), sum frequency generation (SFG), difference frequency generation (DFG) and so on. In these second order processes, a new frequency component is generated as a result of interaction between two incoming photons.

Second harmonic generation is a well-known nonlinear phenomenon which requires a non-centrosymmetric structure under the electric dipole approximation. And because most metals have a face centred cubic unit cell, they are not inherently second harmonic generator. However by introducing nanostructuring, a symmetry breaking can be introduced, giving rise to surface second harmonics [20]. Apart from the dipole approach, electromagnetic field variation can also induce second harmonic, giving way to non-local bulk terms in the nonlinear response of plasmonic structures. Indeed, in plasmonic structures the second harmonic generation should be considered more of a nonlinear scattering process. For better understanding of generation of second harmonic in plasmonic structures, the readers are encouraged to check the detailed hydrodynamic-Maxwell pulse propagation model described in [21,22], which describes the contribution of three competing sources of nonlinear effects (surface, convective and bulk) arising due to both conduction and valence electrons in metals. Without making any initial assumption about separating the surface and bulk nonlinearity, this model relies highly on using the spatial and temporal derivative of the motion of electrons calculated from Newtonian dynamics. They also considered the bulk nonlinearities upto the seventh order which makes more sense in plasmonics because local field intensities can become very high in the edges, enabling the higher order terms.

Plasmonic structures have been the pioneer concept in the research of optically nonlinear

metasurface and nanophotonic structure, due to the strong field enhancement introduced in presence of plasmons. The initial design strategy, as with linear plasmonic metasurface, was to design a gold split ring resonator. This magnetic metamaterial provided a strong nonlinear response in the micrometer regime, arising from the magnetic component of the Lorentz force on the free electrons in metal. The success of this kind of structure comes from exciting the transverse component of SHG, creating a high enhancement in the far-field [23].

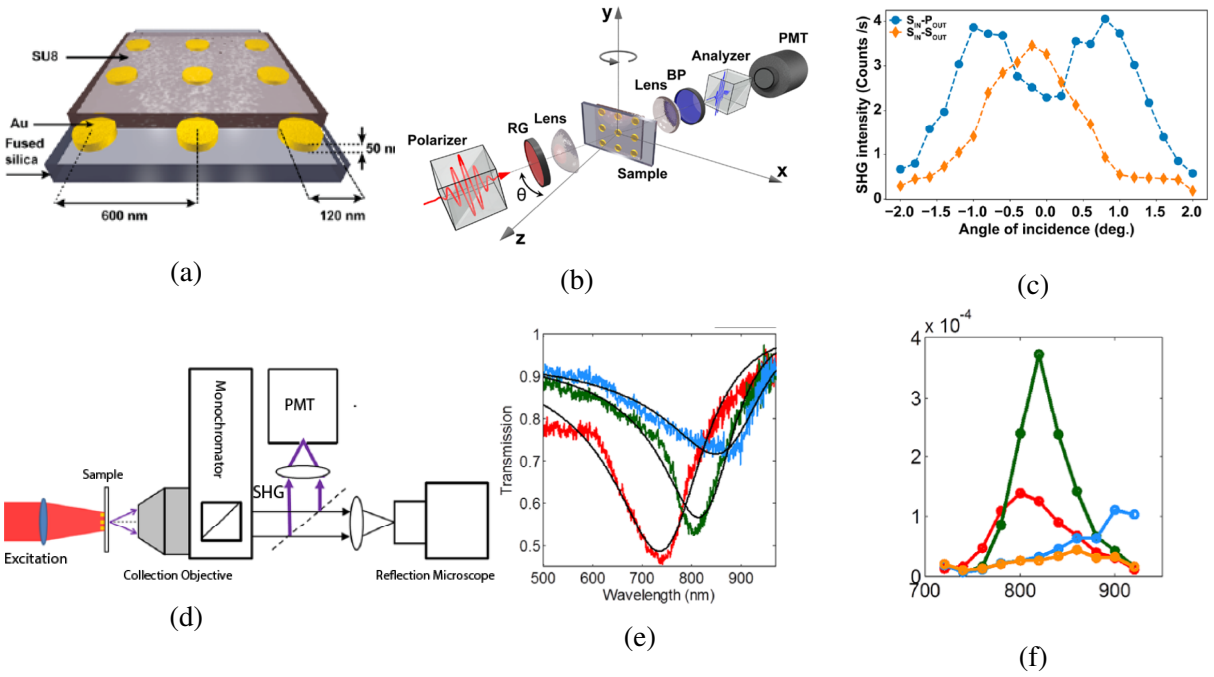

Figure 5. *(a) Array of Au nanoparticles on fused silica substrate, covered in SU8; (b) SHG detection setup in transmission mode and (c) SHG against angle of incidence for two different polarizations, reprinted from [5]. (d) SHG extinction spectroscopy setup; (e) linear and (f) second harmonic spectra for an array of Au nanocylinders, described in [24].*

Beyond the initial strategy of using the field enhancement due to LSPR, strong second harmonic signal has been generated by designing L-shaped metasurfaces resonant at both the fundamental and second harmonic frequencies. Another way to obtain high conversion efficiency (defined as the ratio between the second harmonic power to the fundamental power) has been to use the surface lattice resonances, where an oblique incidence excites the SLR modes and 30 times stronger SLR excitation compared to normal incidence has been reported [25]. In a recent study of SHG in nanoparticle arrays, 450 times SHG enhancement has been reported, along with a narrow linewidth of 5 nm (Figure 5 (a-c)) [5]. This study also reports the separate components of dipolar and quadrupolar SHG component by changing the detection polarization (Figure 5c). SHG from an array of Au nanocylinders (fabricated through electron beam lithography) has also been enhanced by tuning the Fano resonance of the structure (Figure 5(d-f)) [24].

Apart from the nanoparticle structures, nanoholes in films as an inverted system have also been reported based on Babinet's principle. Due to faster heat dissipation in the metal, consequently, higher damage threshold, these nanohole and/or nanocavity structures can endure a higher incident power compared to nanoparticles. Similar to the principle mechanism of SLR, Nieuwstadt et al. studied the SHG response from a hole array as a function of the aspect ratio of the individual holes and upto an order of magnitude enhancement in the effective second order susceptibility was reported at the cutoff aspect ratio, where the cutoff determines where the modes turned from evanescent to propagating [26].

Plasmonic nanorings with a Lithium Niobate filling have also been studied, resulting in 20 times enhancement in the second harmonic compared to only Lithium Niobate nanoparticles of same shape [27]. Enhancement factors upto 10^4 have been achieved using gold nanostructures on an Epsilon-near-zero (ENZ) nanofilm [28], while for silver nanohole substrates, 10^6 fold enhancement have been achieved and used in ultrasensitive imaging [29].

2 Experimental Methodology

2.1 Metasurface Fabrication

Periodic nanostructures were made following a high throughput nanoimprint method. The process involved three consecutive steps: substrate preparation, nanoimprinting and metal deposition.

2.1.1 Substrate Preparation

Commercial Si (001) wafers were chosen as substrates. They were cleaned using first acetone and later isopropyl alcohol (IPA) and thoroughly dried with compressed airflow. For an extensive cleaning of any organic contaminants, O_2 plasma treatment was used for approximately 5 minutes. After cleaning the wafers, around 400 nm layer of 14 wt% SU8 photoresist (MicroChem 2000.5) was deposited through spin-coating for around 30s. The spin speed was kept at 2000 rpm while the acceleration was set at 1000 rpm/s. The wafers were then soft baked at 60°C to evaporate the solvent from the film.

2.1.2 Nanoimprint Lithography

Figure 6a shows the main principle of soft nanoimprint lithography. In this process, a mold or stamp is pressed on a resist to introduce nanoscale deformations, after which the resist is cured to ensure the pattern transfer. Because SU8 is a comparatively malleable substrate and

can be imprinted even at room temperature, it requires only thermal embossing. Therefore the main idea is to heat up the substrate above the glass transition temperature of the resist, slowly apply pressure for prolong periods of time to ensure a homogeneous flow of the resist inside the pattern and have a uniform imprinting at the end. Patterned PDMS stamps for nanohole arrays were already available within the group, which were most used for this work.

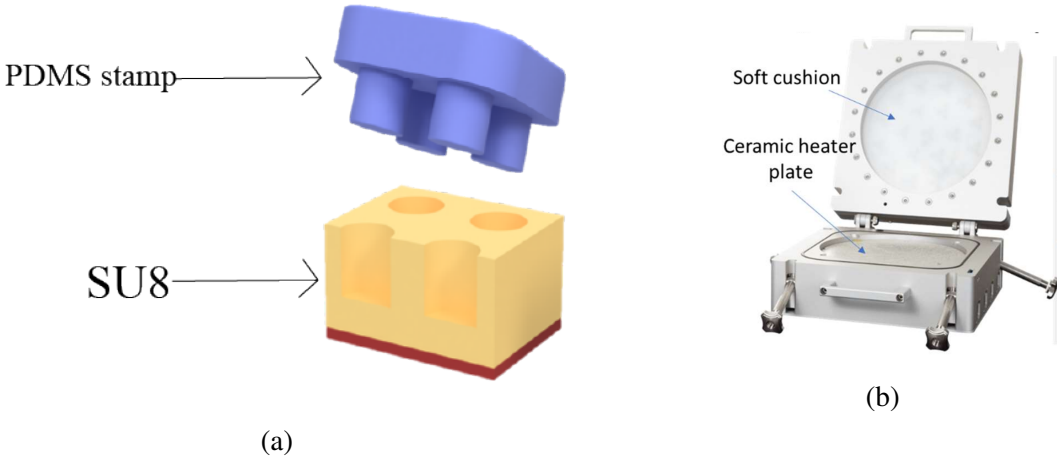

(a) (b)

Figure 6. *(a) Schematic of the imprinting process and (b) the CNI nanoimprint tool used in this experiment for the nanoimprint.*

Figure 6 shows the nanoimprint tool used in this experiment to transfer the patterns in the PDMS molds to the resist substrate. It offers both UV and thermal nanoimprint with a manual loading and unloading, otherwise, completely automated system. The machine supports substrates upto 100 mm diameter and thermal imprint upto 200°C. The attached desktop imprinting software allows precise control of temperature, pressure and imprinting time. The force pressure on the soft stamp is provided through the soft cushion system at the top that inflates through the external compressed air supply. A vacuum pump attachment controls the pressure in the chamber that allows the drying of solvent assisted imprinting process. The ceramic plate at the bottom of the chamber provides the specified temperature, which is also the ceramic stamp carrier. The stamp carrier also works as a very small temperature sensor which has a negligible mass. So, this doesn't interfere with the imprinting but provides an accurate measurement. In typical imprinting, the substrate with the resist film is placed on top of the ceramic plate and the stamp is then placed on top of it, making the resist film sandwiched between the polymer stamp and the substrate. Afterward the machine is closed and high temperature and pressure is applied to engrave the pattern in the polymer stamp into the resist film. The software also allows designing multiple steps with different pressure temperature and duration. For the hot embossing process, the temperature and the pressure of the PDMS stamp pressed into the SU8 substrate are ramped

up to 90°C (glass transition temperature for SU8) and 2 bars, respectively. The setup stays in this configuration for 30s to ensure the pattern is transferred into the substrate. Afterwards the temperature is gradually reduced to 50°C and the pressure is brought back to 1 bar. The mold is then slowly removed from the substrate, taking special precaution to not damage the stamp in the process. After the patterning, the nanostructured resist films are exposed to UV light for 10 minutes for crosslinking and baked at 150°C for 30 minutes to cure the resist and have hard arrays of nanoholes imprinted in them.

2.1.3 Metal Deposition

Metal deposition through thermal evaporation is a well-known technology in the field of nanofabrication. In our case, after the nanopatterns were transferred on the dielectric resist, a thin 50nm layer of gold was deposited on the complete structure using MBraun thermal evaporator, creating a surface completely coated by gold except the walls of the nanoholes. The air pressure inside the evaporator chamber was 10^{-6} bars.

2.2 Linear Characterization

The linear reflectance characterization was done in two steps- first at normal incidence (which gives the maximum resonance) and later as a function of the angle of incidence.

For the normal incidence measurements, a commercial Bruker HYPERION FTIR microscope coupled to a VERTEX 70 spectroscope was used. The source wavelength for this setup can range from visible to NIR range. For our range of interest, we only measured the spectrum from 400 nm to 1200nm wavelength range. The resolution was set to 64cm^{-1} and 100 scans were recorded with a measurement time greater than 13 seconds. The detector was a Si photodiode, captured through a 4x microscope objective. The spot size was around 400X400μm^2. A silver mirror reflecting 96% reflectivity was used as a reference.

The FTIR setup can only measure the reflectance at a normal incidence, so for the dispersion measurement, we moved to a tabletop varying-angle reflection spectroscopy setup. For this, a supercontinuum laser source (FYLA SCT 1000) was used to illuminate the sample with non-polarized light. The sample was mounted on a rotating platform that is also translational in xy axis. The spectrometer used for this section was an AvaSpec 2048 spectrometer with a CMOS detector.

2.3 Second Harmonic Detection

The second harmonic detection setup is shown schematically in Figure 7. The incoming fundamental beam is from a Ti:Sapphire femtosecond laser with the center wavelength at 800 nm, pulse duration 170 fs at a 76 MHz repetition rate with a continuous wave output of 1.3 W. The half waveplate at the input is used to control the polarization of the incoming light. After the waveplate, longpass filters are used to eliminate any sort of higher harmonics produced in the optics from the fundamental beam. A collimating lens of 100 mm focal length was used to focus the light beam on the sample with a spot size of 40 μm.

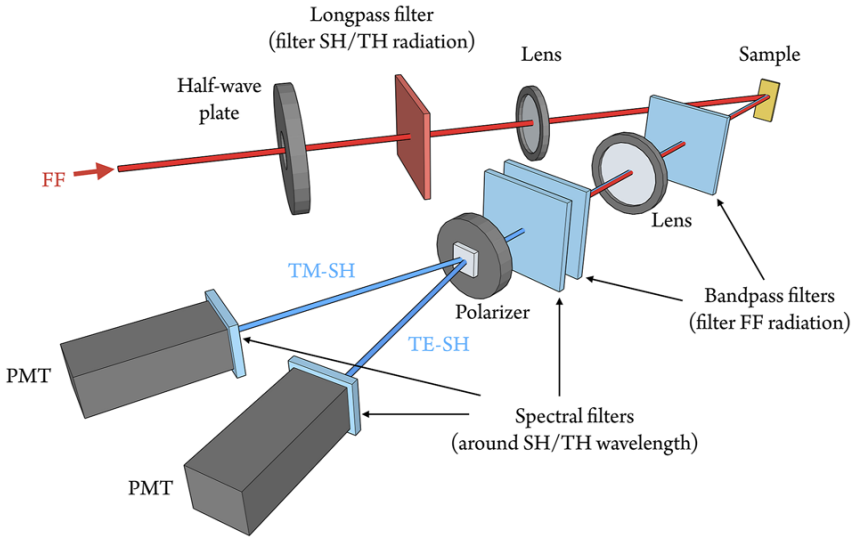

Figure 7. *Schematic for the experimental setup used to detect the reflected second harmonic signal generated by the metasurface as a function of the angle of incidence and polarization of the light, reproduced from [22].*

The samples are placed on a rotary stage that has an angular resolution of 0.2° and this sample holder is placed before another bandpass filter at 400 nm center wavelength and 40nm bandwidth that ensures that the signal passing after the sample is strictly the second harmonic and not the input signal. To collimate the signal generated in the sample, a lens is used in the detection arm. Because the filtering of SH signal is the most crucial part in this detection, another set of bandpass filters are added after the collimating lens. One of these filters are directly placed before the PMT detector. A Wollaston polarizer is added before the PMT to separate the harmonic signal into its TE and TM component. The detection system after the sample is placed on a rotating tail, which allow a variation of incident angle to be measured. However, our current setup does not allow the measurement of the second harmonic at the normal incidence since the detection setup blocks the input in that case.

A detailed alignment and calibration process was carried out for this detection setup. To

ensure the alignment, a strong second harmonic signal was generated using a beta barium borate (BBO) crystal. With the help of this BBO assisted second harmonic, it was also checked that the signal at the PMT is changing as a function of the fundamental power and indeed is the second harmonic. The PMT was powered by an external control voltage source and the gain for the PMT was accounted for depending on this control voltage. For a full precise measurement, the PMT responsivity has to be calculated at the second harmonic wavelength using a 405 nm laser source and power meters. To calculate the conversion efficiencies, the transmittance of the filters and lenses after the sample also have to be accounted for. A chopper was also included right after the input laser to supply a square waveform in order to facilitate second harmonic detection.

3 Results and Discussions

3.1 Square Lattice Array

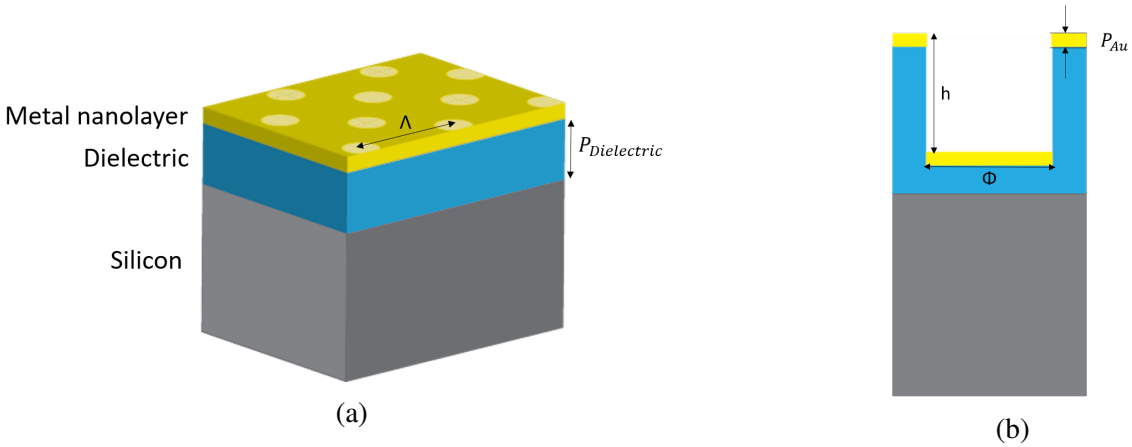

Figure 8. *(a) Schematic of the fabricated structure used in this experiment: square lattice of nanohole arrays with lattice parameter, Λ and hole diameter, Φ and (b) Cross-sectional view of a nanohole in the array. The gold layer was deposited after the nanoimprinting, creating a homogeneous gold layer at the top and bottom faces of the nanoholes but not along the hole depth.*

The design of the metasurface fabricated for this work is shown in Figure 8. Uniform gold coating of around 50 nm were deposited, covering both the raised and depressed regions with gold. The final structure is thus an array of nanoholes in a metal film as well as a periodic array of gold nanodisks, creating a quasi 3D plasmonic crystal. The lattice parameter of the array is denoted by Λ, the individual hole diameter by Φ and the hole depth in the dielectric layer is h. The dielectric layer and the metal nanolayer thickness are $P_{dielectric}$ and P_{Au}, respectively. The top face of the gold nanodisks at the depressions and the bottom face of the upper gold

film creates a Fabry-Perot resonator, resulting in a strong light confinement [30]. This kind of structure supports multiple resonances, which has been known to be an advantageous approach in order to generate second harmonic from plasmonic structures [31]. In these structures, different kinds of resonances overlap: LSPR from the rim of the upper gold holes and the gold disks at the bottom of the depression, the Wood's anomalies and the Bloch wave surface plasmon polaritons, which are standing waves that stems from the superimposing propagating SPPs, also resulting from the periodicity of the holes [32].

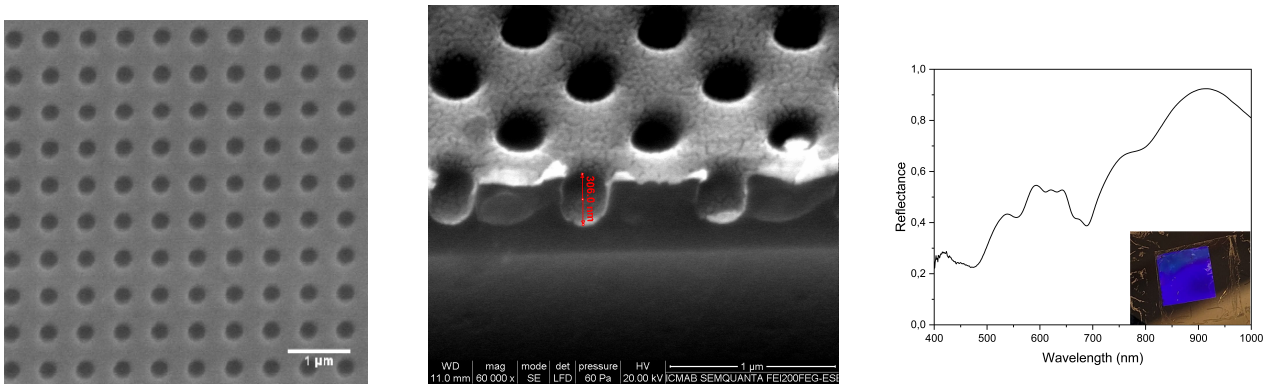

(a) (b) (c)

Figure 9. *SEM image of one of our fabricated samples with predefined parameters of (a) lattice parameter 600 nm and 338 nm hole diameter with (b) a depth of around 390 nm. (c) shows the reflectance spectra of the array, the inset shows the nanohole array.*

A set of such metasurface fabricated using prepatterned PDMS stamps is shown in Figure 9. The parameters specified were the following: the lattice parameter 600 nm and the hole diameter 338 nm and the hole depth was 390 nm. Scanning electron microscope (SEM) images show a lattice parameter of 600 ± 4 nm, the hole diameter was around 280 ± 4 nm and the depth was 306 ± 2 nm. This indicates the pattern is replicated accurately spaced but the individual holes didn't retain the original diameter during the imprinting process. The reflectance spectra (Figure 9c) shows the lattice resonance wavelength to be in the range of 650-700 nm. Another broad resonance is also visible at around 471 nm, which might be due to the LSPR.

3.1.1 Effect of Lattice Parameter

Next, to observe the effects of lattice parameter we used a multipattern stamp, containing lattice parameters with a short interval of 20 nm each. All of these samples have a hole depth of around 100 nm. The geometrical parameters are as follows:

- Sample 1: $\Lambda - 720nm; \Phi - 420nm$

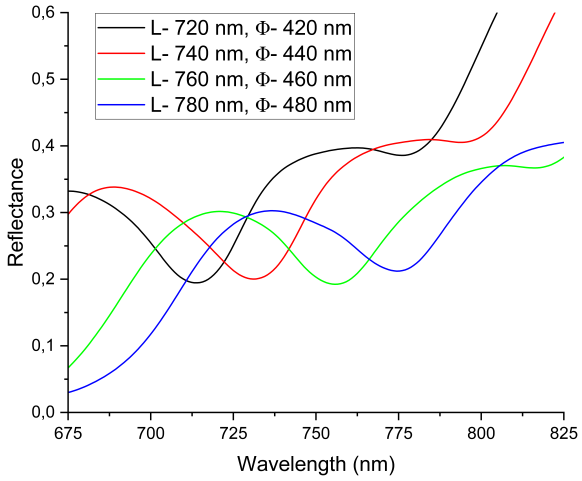

Figure 10. *Reflectance spectra of metasurfaces with lattice parameters of 720 nm, 740 nm, 760 nm and 780 nm. The hole diameters also increase by 20 nm in each sample, starting from 420nm and ending in 480 nm.*

- Sample 2: $\Lambda - 740nm; \Phi - 440nm$
- Sample 3: $\Lambda - 760nm; \Phi - 460nm$
- Sample 4: $\Lambda - 780nm; \Phi - 480nm$

The reflectance spectra are shown in Figure 10. The resonance positions were 714nm, 732 nm, 756 nm and 774 nm, respectively. The wavelengths are in good agreement with the surface lattice resonant wavelength due to the grating behavious of the nanohole arrays. The resonant wavelength shift was $\Delta\lambda = 20 \pm 0.5$ nm for a 20 nm change in the diameter of the lattice parameters. However, the resonances were quite broad, with an FWHM around 28.2±0.75 nm.

3.1.2 Effect of Dielectric Environment

The quality factor (Q-factor) of a resonance is defined by:

$$Q - factor = \frac{\lambda_{max}}{FWHM} \tag{6}$$

where λ_{max} is defined as the resonant wavelength, and FWHM is the full width half maximum of the strongest resonance. The Q-factor is a measurement of the definition or the strength of the resonance, and therefore a parameter to indicate the strength of light confinement.

To improve the quality factor of the resonance, we spin-coated another layer of SU8 of 400 nm to provide a refractive index-matched (IM) environment. As expected, the homogeneous re-

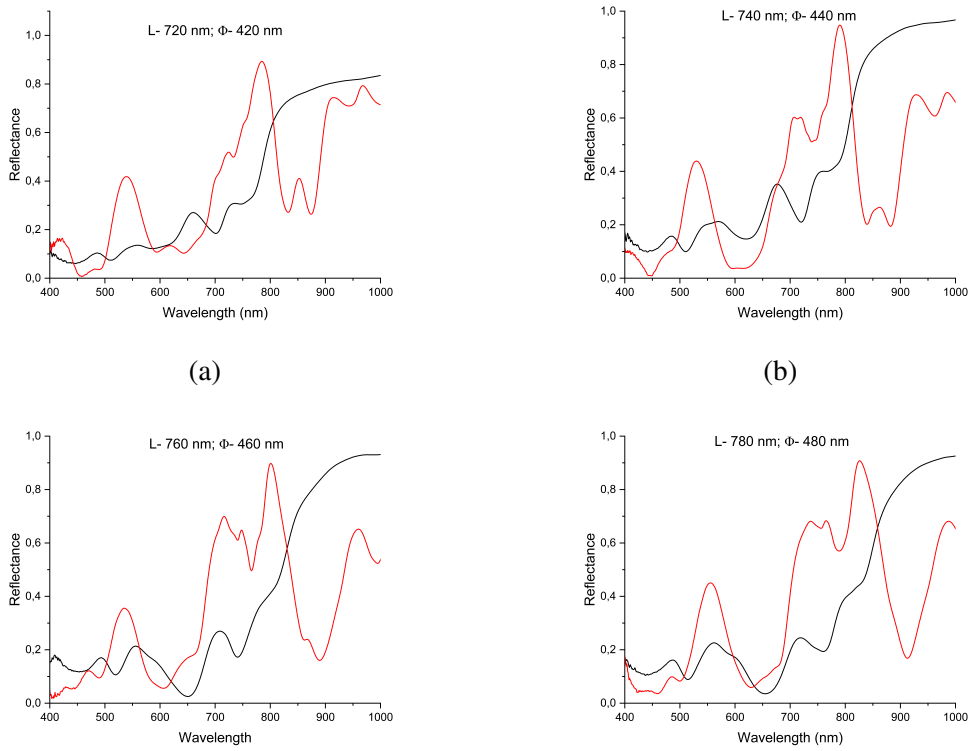

Figure 11. *Effect of index-matching in reflectance spectra of the metasurfaces for lattice parameters of (a) 720 nm, (b) 740 nm, (c) 760 nm and (d) 780 nm. The black lines show the original samples with air($\eta_1 = 1$) as superstrate and SU8($\eta_2 = 1.59$) as substrate. The red lines indicate the index-matched environment with coating the structures in SU8 on both sides.*

fractive index environment gave a sharper resonance overall, while also shifting the resonance position to a higher wavelength. The qualitative explanation for this depth can be explained by the radiation pattern. In case of a non-index matched environment, the radiation pattern is highly asymmetric where most of the light scatters inside the high refractive index substrate. Therefore the lattice resonances in such environments are weaker. However, in an index-matched environment, the radiation pattern is symmetrically distributed over both the substrate and the superstrate, generating a much higher coupling of the diffracted zeroth order into in-plane scattered light [33]. The redshift is due to the increased refractive index around the metasurface. Apart from the spectral red-shift, another thing to notice in Figure 11 is that in the index-matched samples, the resonances are often split into two small dips, and there are also some extra peaks appearing, which can be attributed to the guided mode resonances in the gold layer.

3.1.3 Angular Dispersion

In order to experimentally retrieve the dispersion relationship of the SLR in our structures, we obtained the reflectance spectra with an increasing angle of incidence for sample 3 ($\Lambda - 760nm, \Phi - 460nm$) with an index matched layer of SU8 photoresist on top of the gold structures. The results are shown in Figure 12.

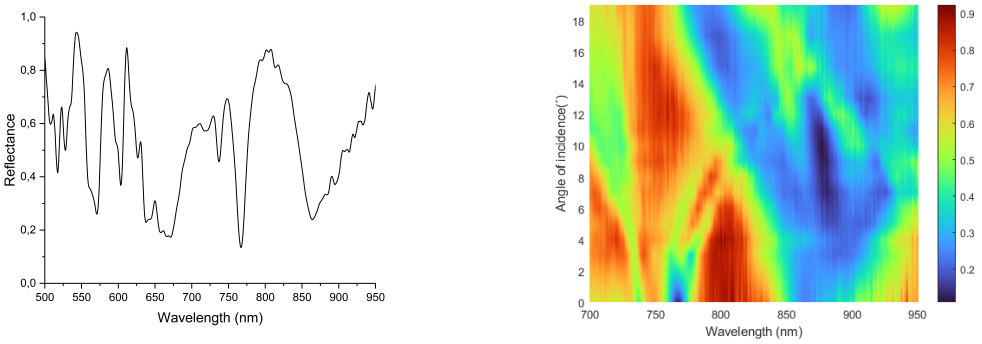

(a) (b)

Figure 12. *(a) Normal incidence spectra and (b) angular dispersion of a square lattice nanohole array with periodicity* $\Lambda - 760$ *nm and hole diameter* $\Phi - 460$ *nm with a refractive index matched environment* ($\eta_1 = \eta_2 = 1.59$).

Figure 12a shows the normal incidence spectra for the sample where a clear resonance at 766 nm can be visible. However, moving to higher angles show a very strong decline in this resonance, which can be observed in Figure 12b. The reflectance map in Figure 12b showed this strong resonance to split and later disappear at 4° angle. Another branch of resonance, originating at 850-900 nm wavelength range, shows splitting in multiple components with higher angles.

3.1.4 Second Harmonic Detection

The reflectance map in Figure 12b, showed a weak but broad resonance branch at 800 nm, starting at 10° and extending upto 19°. The second harmonic signal was measured in this angular range, the experimental results are shown in Figure 13a. For our set of measurements, we detected the TM polarized second harmonic signal for a TM polarized fundamental signal. The measurements were done against a varying angle of incidence. The input power was set at 1.3 Watts.

The highest conversion efficiency for the second harmonic signal was achieved for a 15.5° incident beam. As the angles deviate from the highest resonance angle, the SHG enhancement keeps decreasing and vanishes for a higher angle from resonance. Compared to the flat gold layer, the maximum enhancement factor reached for this structure was 16.09. While this enhancement

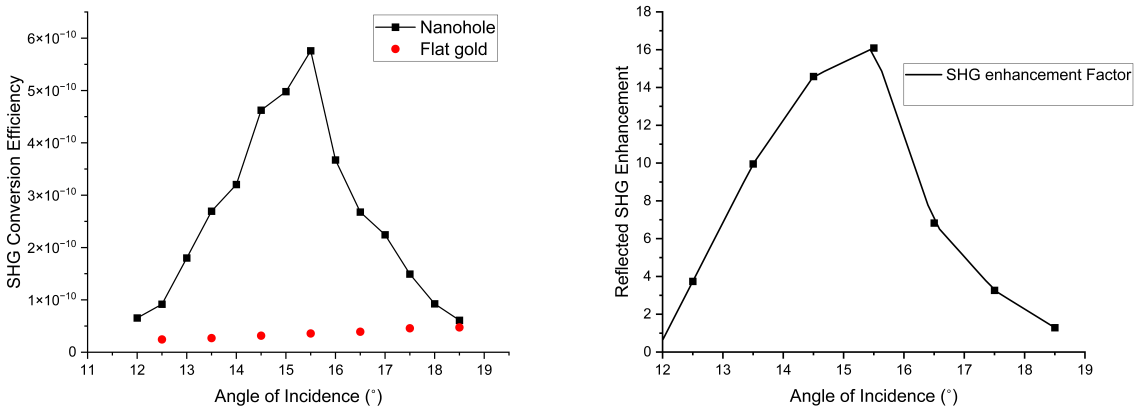

(a) (b)

Figure 13. *(a)The SHG conversion efficiency and (b) the enhancement factor as a function of angle of incidence for the nanohole array shown in Figure 12.*

is much lower than the ones previously reported ones in 1D gratings [22], this is clearly not the highest obtainable second harmonic signal from these kind of structures. For our structure, the Q-factor of the resonance at 15.5° is 17, while at normal incidence it increases up to 49.17. Measurement of second harmonic at normal incidence will thus, result in a higher signal. For this purpose, the setup modification is already underway, where a beam splitter with a 40 nm bandwidth at 400 nm wavelength will detect the normal incidence SHG. Furthermore, the second harmonic at 400 nm with this periodicity will generate multiple diffraction order, while the detected signal in Figure 13 only takes into consideration the zeroth order emission, making this measurement an initial insight into the light confinement by the metasurface but by no means the complete picture.

3.2 Hexagonal Lattice Array

Another set of samples with a similar schematic to Figure 8 but with a hexagonal lattice pattern was prepared using the same method described in Section 2.1 using PDMS molds with prepatterned areas of $1cm^2$. The corresponding SEM image and the reflectance spectra are shown in Figure 14.

Comparing Figure 14b to Figure 9c, we can observe that for a different geometric configuration, there is still a resonance at 491 nm, which is the LSPR from the gold nanostructuring. Furthermore, there are more resonances arising from the periodicity of the lattice present as multiple waves in the reflectance spectrum in the range of 660-745 nm.

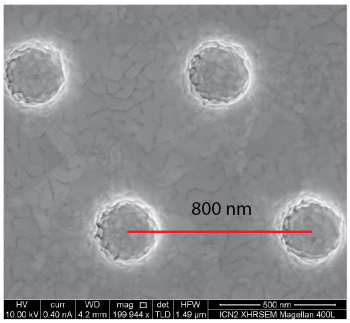

(a)

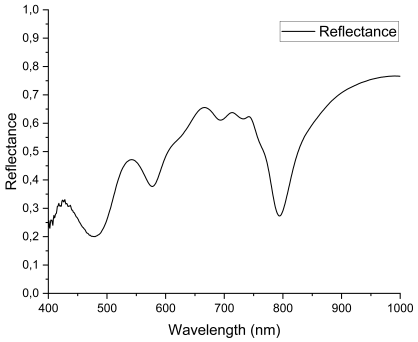

(b)

Figure 14. *(a) SEM image of a hexagonal nanohole array with lattice parameter* Λ – 800 *nm and (b) the corresponding reflectance spectrum.*

3.2.1 Effect of Lattice Parameter

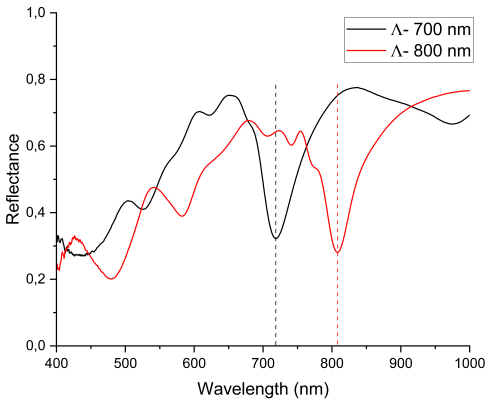

Figure 15. *Reflectance spectra of two different lattice parameters in case of hexagonal patterning.*

Figure 15 shows the reflectance spectra for two different metasurfaces with lattice parameters, Λ_1 = 700 nm and Λ_2 = 800 nm. The zero order resonance was at 718.28 nm and 795 nm, respectively. Again in this case, the resonance position is tuned according to the geometrical parameter of the sample itself, with the wavelength shift, $\Delta\lambda$ = 76.72 nm for a lattice parameter shift of 100 nm.

3.2.2 Angular Dispersion

The angular dispersion plot for this structure is presented in Figure 16.

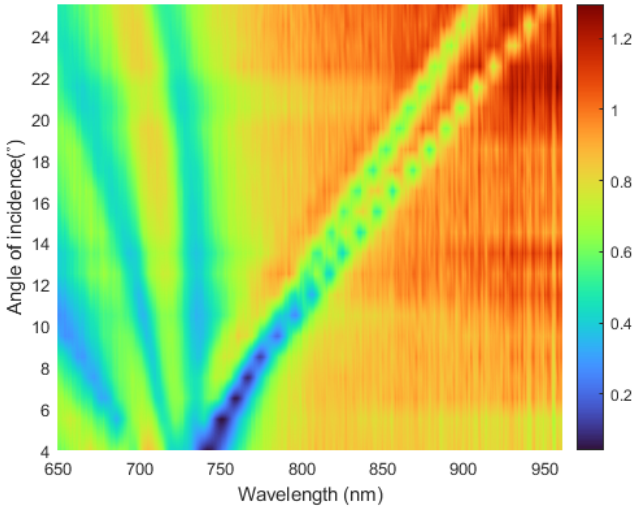

Figure 16. *The angular dispersion of the reflectance of the hexagonal array with lattice parameter,* $\Lambda = 800$ *nm and hole diameter,* $\Phi = 300$ *nm.*

The angular response of hexagonal patterning is significantly different from square one. The hexagonal structure shows a strong angular dispersion with significant mode splitting. Here the resonance branch sustains over a higher angle and splits into two distinct small resonances, which also redshift with increasing angle and vanish at around 20°. This difference is due to the different reciprocal vector lengths associated with hexagonal unit cells, which influences the coupling of incident light to surface waves. In case of an increasing angle, the incident in-plane light component along the different lattice axes varies significantly, resulting in a strong mode splitting.

4 Conclusion

To conclude, we have fabricated and engineered metasurfaces resembling a quasi 3D plasmonic crystals to observe enhanced light-matter interaction through an experimental detection of second harmonic signal. Our approach is to use soft nanoimprint lithography which is a scalable and versatile fabrication process, allowing us access to an abundance of possible structures to implement. We have demonstrated the effect of lattice parameter, dielectric environment, array geometry on the multiple resonances supported by the metasurfaces. Because of the complex nature of the resonances sustained by this kind of structures, it is hard to formulate a straightforward relation between the geometric parameters and the resulting resonances. Our structures have shown more resonances in hexagonal arrays of cylindrical depressions in comparison to square arrays.

In case of square lattice array, the zero order resonance from the metasurface, occuring at

the same wavelength corresponding to the lattice period, is showed to follow the lattice parameter closely in every case. However in a hexagonal patterning of the holes, this resonance was redshifted by $\Delta\lambda = 18 \pm 0.05$ nm for a 700 nm lattice parameter. The lattice parameters were confirmed by SEM imaging. In contrast to an inhomogeneous dielectric environment, an index-matching has shown to result in sharper but redshifted resonances, making a compromise in terms of Q-factor.

As an experimental verification of the light confinement, we have also demonstrated nonlinear phenomena occuring even at a non-ideal condition. A highest conversion efficiency of $5.76 \times 10^{-11}\mathrm{W}^{-1}$ was achieved in the index-matched metasurface with 760 nm lattice spacing. We found a 16 fold enhancement in the second harmonic signal generated in the patterned region of the metasurface compared to the gold film. This enhancement is limited by the current setup, where the excitation wavelength tunability and the accessible detection angle both are restricted to a small range. In any case, the angular dispersion measurements show the potential to obtain higher conversion efficiencies through (a) changing the excitation wavelength to the resonance wavelengths having high Q-factor, (b) using the hexagonal lattice samples and (c) measuring the second harmonic at normal incidence. For a full nonlinear characterization, the next step is to measure the second harmonic at normal incidence, which is going to be collected through a modification in the existing setup. Further, a higher angular range detection would ensure the collection of multiple diffraction orders, which is a prominent effect in case of 2D arrays. From a fabrication point of view, designing a metasurface resonant both at the fundamental and second harmonic frequency will allow us stronger second harmonic signal, giving us more insight into the relationship between linear and nonlinear response in plasmonic systems.

Acknowledgements. My heartfelt gratitude to Dr. Viktorija Tamulienė for reviewing this thesis multiple times and also for the necessary administrative support. Special thanks to prof. Crina Cojocaru for her warm welcome in the group and always being a person to rely upon, Dr. Jose Trull for his invaluable expertise and excellent explanations in the lab and Dr. Agustin Mihi for hosting me at ICMAB-CSIC. Thanks to Shroddha Mukhopadhyay for her help in the nonlinear experiments in this thesis. Furthermore, I would like to thank everyone at the NANOPTO group at ICMAB-CSIC for helping me whenever I reached out and teaching me things beyond what this thesis covers, with special mentions to Reyda Akdemir for being the absolute best mentor as well as a great friend, and José Mendoza Carreño for always taking the time out of his schedule to share both his theoretical and practical expertise with me.

References

[1] C. Wang, Y. Wen, J. Sun, and J. Zhou, Recent progress on optical frequency conversion in nonlinear metasurfaces and nanophotonics, *ES Materials & Manufacturing*, 2022, **17**, 1–13.

[2] E. Yablonovitch, Photonic crystals: semiconductors of light, *Scientific American*, 2001, **285**, 46–55.

[3] M. Z. Alam, S. A. Schulz, J. Upham, I. De Leon, and R. W. Boyd, Large optical nonlinearity of nanoantennas coupled to an epsilon-near-zero material, *Nature Photonics*, 2018, **12**, 79–83.

[4] D. de Ceglia, M. A. Vincenti, N. Akozbek, M. J. Bloemer, and M. Scalora, Nested plasmonic resonances: extraordinary enhancement of linear and nonlinear interactions, *Optics Express*, 2017, **25**, 3980–3990.

[5] D. C. Hooper, C. Kuppe, D. Wang, W. Wang, J. Guan, T. W. Odom, and V. K. Valev, Second harmonic spectroscopy of surface lattice resonances, *Nano letters*, 2018, **19**, 165–172.

[6] N. Bloembergen, R. K. Chang, S. Jha, and C. Lee, Optical second-harmonic generation in reflection from media with inversion symmetry, *Physical Review*, 1968, **174**, 813.

[7] H. Ghaemi, T. Thio, D. e. a. Grupp, T. W. Ebbesen, and H. Lezec, Surface plasmons enhance optical transmission through subwavelength holes, *Physical review B*, 1998, **58**, 6779.

[8] D. Pines, Collective energy losses in solids, *Reviews of modern physics*, 1956, **28**, 184.

[9] M. Cardona and G. Güntherodt, Light scattering in solids iv: Electronics scattering, spin effects, sers, and morphic effects, 1984.

[10] S.-Q. Li, P. Guo, D. B. Buchholz, *et al.*, Plasmonic–photonic mode coupling in indium-tin-oxide nanorod arrays, *ACS Photonics*, 2014, **1**, 163–172.

[11] J. M. Luther, P. K. Jain, T. Ewers, and A. P. Alivisatos, Localized surface plasmon resonances arising from free carriers in doped quantum dots, *Nature materials*, 2011, **10**, 361–366.

[12] E. Kretschmann and H. Raether, Radiative decay of non radiative surface plasmons excited by light, *Zeitschrift für Naturforschung A*, 1968, **23**, 2135–2136.

[13] R. H. Ritchie, E. Arakawa, J. Cowan, and R. Hamm, Surface-plasmon resonance effect in grating diffraction, *Physical review letters*, 1968, **21**, 1530.

[14] S. A. Maier *et al.*, *Plasmonics: fundamentals and applications*, vol. 1. Springer, 2007.

[15] D. L. Mills and V. M. Agranovich, *Surface polaritons: electromagnetic waves at surfaces and interfaces*. North-Holland Publ., 1982.

[16] W. Wang, M. Ramezani, A. I. Väkeväinen, P. Törmä, J. G. Rivas, and T. W. Odom, The rich photonic world of plasmonic nanoparticle arrays, *Materials today*, 2018, **21**, 303–314.

[17] V. G. Kravets, A. V. Kabashin, W. L. Barnes, and A. N. Grigorenko, Plasmonic surface lattice resonances: a review of properties and applications, *Chemical reviews*, 2018, **118**, 5912–5951.

[18] P. Molet, N. Passarelli, L. A. Pérez, L. Scarabelli, and A. Mihi, Engineering plasmonic colloidal meta-molecules for tunable photonic supercrystals, *Advanced Optical Materials*, 2021, **9**, 2100761.

[19] R. W. Boyd, *Nonlinear optics*. Academic press, 2020.

[20] H. Lu, X. Liu, R. Zhou, Y. Gong, and D. Mao, Second-harmonic generation from metal-film nanohole arrays, *Applied optics*, 2010, **49**, 2347–2351.

[21] L. Rodríguez-Suné, J. Trull, C. Cojocaru, N. Akozbek, D. De Ceglia, M. Vincenti, and M. Scalora, Harmonic generation from gold nanolayers: bound and hot electron contributions to nonlinear dispersion, *Optics express*, 2021, **29**, 8581–8591.

[22] S. Mukhopadhyay, L. Rodriguez-Suné, C. Cojocaru, *et al.*, Three orders of magnitude enhancement of second and third harmonic generation in the visible and ultraviolet ranges from plasmonic gold nanogratings, *APL Photonics*, 2023, **8**.

[23] M. W. Klein, C. Enkrich, M. Wegener, and S. Linden, Second-harmonic generation from magnetic metamaterials, *Science*, 2006, **313**, 502–504.

[24] G. F. Walsh and L. Dal Negro, Enhanced second harmonic generation by photonic–plasmonic fano-type coupling in nanoplasmonic arrays, *Nano letters*, 2013, **13**, 3111–3117.

[25] L. Michaeli, S. Keren-Zur, O. Avayu, H. Suchowski, and T. Ellenbogen, Nonlinear surface lattice resonance in plasmonic nanoparticle arrays, *Physical review letters*, 2017, **118**, 243904.

[26] J. Van Nieuwstadt, M. Sandtke, R. Harmsen, F. B. Segerink, J. Prangsma, S. Enoch, and L. Kuipers, Strong modification of the nonlinear optical response of metallic subwavelength hole arrays, *Physical review letters*, 2006, **97**, 146102.

[27] D. Lehr, J. Reinhold, I. Thiele, *et al.*, Enhancing second harmonic generation in gold nanoring resonators filled with lithium niobate, *Nano letters*, 2015, **15**, 1025–1030.

[28] J. Deng, Y. Tang, S. Chen, K. Li, A. V. Zayats, and G. Li, Giant enhancement of second-order nonlinearity of epsilon-near-zero medium by a plasmonic metasurface, *Nano Letters*, 2020, **20**, 5421–5427.

[29] S. P. Sahu, A. Mahigir, B. Chidester, G. Veronis, and M. R. Gartia, Ultrasensitive three-dimensional orientation imaging of single molecules on plasmonic nanohole arrays using second harmonic generation, *Nano letters*, 2019, **19**, 6192–6202.

[30] J. Xu, P. Guan, P. Kvasnicka, H. Gong, J. Homola, and Q. Yu, Light transmission and surface-enhanced raman scattering of quasi-3d plasmonic nanostructure arrays with deep and shallow fabry-perot nanocavities, *The Journal of Physical Chemistry C*, 2011, **115**, 10996–11002.

[31] J. Butet, P.-F. Brevet, and O. J. Martin, Optical second harmonic generation in plasmonic nanostructures: from fundamental principles to advanced applications, *ACS nano*, 2015, **9**, 10545–10562.

[32] M. E. Stewart, N. H. Mack, V. Malyarchuk, *et al.*, Quantitative multispectral biosensing and 1d imaging using quasi-3d plasmonic crystals, *Proceedings of the National Academy of Sciences*, 2006, **103**, 17143–17148.

[33] D. Khlopin, F. Laux, W. P. Wardley, *et al.*, Lattice modes and plasmonic linewidth engineering in gold and aluminum nanoparticle arrays, *JOSA B*, 2017, **34**, 691–700.

Building Plasmonic Crystals from Gold Nanoimprinted Metasurfaces

Fariha Binte Rahman

Summary

Due to their extraordinary light confinement properties, plasmonic metasurfaces have attracted much attention in applications in the visible and IR range. Apart from the multitude of applications using the linear transmission properties, the intensity build-up in subwavelength volumes have emerged as an excellent way to observe nonlinear phenomena. The fabrication of the nanoscale structures following the traditional methods, however, still is a cumbersome process. In this work, we fabricated multiple quasi-3D plasmonic crystals via soft nanoimprint lithography, allowing us access to nanoscale variation of structural parameters with an easy scalable fabrication process. We observed the effects on surface lattice resonances as a function of varying lattice parameter, dielectric environment as well as array geometry. While the index-matching has resulted in a sharper resonance, the redshift of the resonances have resulted in a lower energy confinement. We have also experimentally reported the angular dispersion of the surface lattice resonance in both square and hexagonally arranged metasurfaces. Finally, as an initial proof of light confinement in our structures, we have detected the second harmonic signal generated from these metasurfaces, giving us 16 fold enhancement compared to the flat gold surface. To our knowledge, second harmonic generation from quasi-3D plasmonic crystals haven't been studied, and the linear properties obtained via this study show the necessary improvements to follow in this project.